Surface Control of Epitaxial Manganite Films *via* Oxygen Pressure

Alexander Tselev,* Rama K. Vasudevan, Anthony G. Gianfrancesco, Liang Qiao,† P. Ganesh, Tricia L. Meyer, Ho Nyung Lee, Michael D. Biegalski, Arthur P. Baddorf, and Sergei V. Kalinin*

Oak Ridge National Laboratory, Oak Ridge, Tennessee 37831, United States. †Present address: School of Materials, The University of Manchester, Grosvenor Street, Manchester M13 9PL, U.K.

ABSTRACT The trend to reduce device dimensions demands increasing attention to atomic-scale details of structure of thin films as well as to pathways to control it. This is of special importance in the systems with multiple competing interactions. We have used *in situ* scanning tunneling microscopy to image surfaces of $La_{5/8}Ca_{3/8}MnO_3$ films grown by pulsed laser deposition. The atomically resolved imaging was combined with *in situ* angle-resolved X-ray photoelectron spectroscopy. We find a strong effect of the background oxygen pressure during deposition on structural and chemical features of the film surface. Deposition at 50 mTorr of O_2 leads to mixed-terminated film surfaces, with B-site (MnO_2) termination being structurally imperfect at the atomic scale. A relatively small reduction of the oxygen pressure to 20 mTorr results in a dramatic change of the surface structure leading to a nearly perfectly ordered B-site terminated surface with only a small fraction of A-site (La,Ca)O termination. This is accompanied, however, by surface roughening at a mesoscopic length scale. The results suggest that oxygen has a strong link to the adatom mobility during growth. The effect of the oxygen pressure on dopant surface segregation is also pronounced: Ca surface segregation is decreased with oxygen pressure reduction.

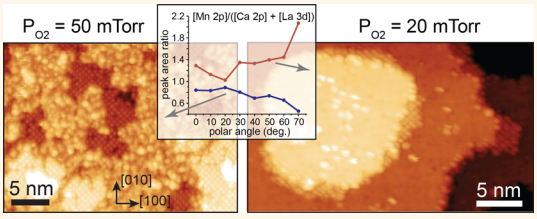

KEYWORDS: perovskite manganite · pulsed laser deposition · scanning tunneling microscopy · X-ray photoelectron spectroscopy · surface structure

Because of strong electron–electron correlations and electron–lattice coupling, electronic and magnetic properties of mixed valence manganites with perovskite structure (with a general formula $A_{1-x}A'_xBO_3$, where A is a rare-earth cation, A′ is an alkali or alkaline earth cation, and B is occupied by Mn) are governed by the complex interplay and competition between interactions in lattice, charge, orbital, and spin degrees of freedom.[1,2] This leads to complex phase diagrams and a strong dependence of the transport and magnetic behavior on various external and internal factors including chemical and structural disorder, doping, oxygen stoichiometry, temperature, strain, electric and magnetic fields.[1−6] In particular, manganites exhibit metal–insulator transitions, colossal magnetoresistance, charge ordering and varying magnetic structures, as well as nanoscale phase separation.[1,2] The multitude of phenomena inherent to these compounds lead to significant research efforts in the past two decades in order to obtain a fundamental understanding and further harness this complexity to obtain novel functionalities for applications such as in electronics and spintronics, especially in the form of thin films and thin film heterostructures.[4,7−14] More recently, Manganite thin films were shown to be amenable to electroforming and to have application in resistive switching devices.[15] Finally, due to a high electrical conductivity and a good chemical and thermal match with solid electrolytes, Sr-doped $LaMnO_3$ (LSMO) is widely utilized for cathode materials in solid-oxide fuel cells.[16]

The functionality of thin-film and heterostructure electronic devices is strongly dependent on electronic structure and properties of surfaces and interfaces. This becomes of increasing importance with reduction of the device dimensions and film thickness. Behavior and interaction of magnetic, lattice, and charge order parameters at the surface can be drastically changed in comparison with the bulk due to symmetry breaking, reduction in number of atomic

* Address correspondence to tseleva@ornl.gov, sergei2@ornl.gov.

Received for review February 2, 2015 and accepted March 10, 2015.

Published online March 11, 2015
10.1021/acsnano.5b00743

bonds, and surface atomic reconstructions or extrinsic mechanisms associated with cation nonstoichiometry and structure defects.[8,17−24] In turn, catalytic and electrochemical reactions are largely dependent on atomic-scale structure and processes at oxide surfaces.[25] It is apparent that knowledge-based control of Manganite thin film and heterostructure growth with understanding of the atomic-scale mechanism of surface structure formation is necessary.

In this work, we grew films of a hole-doped Manganite $La_{5/8}Ca_{3/8}MnO_3$ (LCMO) *via* pulsed laser deposition (PLD) and characterized them by *in situ* scanning tunneling microscopy (STM) in combination with *in situ* angular-resolved X-ray photoelectron spectroscopy (AR-XPS). The combination of film growth followed by *in situ* STM and XPS measurements allowed access to real-space atomic structure of the film surface with detailed information on the terminations and surface chemical composition. PLD allows atomic-level control of layer thicknesses and interfaces and is most commonly used for fabrication of perovskite oxide-based structures for about two decades. However, because of significant experimental difficulties associated with STM imaging of PLD-grown films, atomically resolved *in situ* STM has only recently been implemented to study PLD film growth, resulting in important insights into atomic-scale surface morphology and growth kinetics.[26−31] On the other side, while highly beneficial in general, atomically resolved STM studies of manganites have been so far rare. With a few notable exceptions, when surfaces of perovskite single crystals were imaged after simple cleaning with solvents,[32,33] the atomic resolution could be only achieved with single crystals of bilayered manganites, which can be cleaved *in situ*.[34,35]

LCMO is a prototypical colossal magnetoresistive material.[36] It exhibits growth behavior and thin film features similar to the closely related Lanthanum Strontium Manganese Oxide (LSMO) primarily used in device structures (owing to its higher Curie temperature of about 370 K). Because of a smaller size mismatch between Ca^{2+} dopant ions and parent La^{3+} ions, LCMO is less prone to dopant surface segregation than LSMO.[37] Surfaces of PLD-grown LCMO films were previously studied with atomically resolved STM, and the studies revealed that surface electronic properties can be changed from metallic to insulating by only one monolayer of adsorbed oxygen.[38] LCMO was also employed to uncover important atomic-scale aspects of the substrate−film interaction in PLD growth.[31] Here, we focused on the role of the background oxygen pressure on growth kinetics, atomic-scale surface structure, and surface chemical composition of LCMO films.

The critical role of background oxygen pressure during PLD deposition in properties of Manganite thin films and heterostructures is well-established in many experiments, where film properties were followed as a function of oxygen pressure.[39−41] A common thought supported by analytical work is that a higher oxygen pressure is needed to compensate for oxygen deficiency, improve cationic stoichiometry, and reduce structural damage due to resputtering of the deposited film by highly energetic plasma species.[41−43] While an optimal pressure close to 200−300 mTorr is usually cited for Manganite films, counterintuitively, Song *et al.*[39] and confirmed by Kourkoutis *et al.*[17] have discovered that significantly lower pressure levels—1 mTorr and down to 10^{-6} Torr—can be highly beneficial for structural and physical properties of Manganite films and interfaces in heterostructures, provided that the laser fluence is reduced to decrease the kinetic energy of particles in the deposition flux.

In this study, we found the existence of a borderline oxygen pressure in the range between 20 mTorr and 50 mTorr during the growth of LCMO films on TiO_2-terminated $SrTiO_3$ (001) substrates. We observed dramatic changes in the surface structure at mesoscopic and atomic levels, and hence, in growth dynamics with relatively small change of the oxygen pressure. The observed modification of the growth behavior is proposed to occur due to dependence of the effective mobility of Mn adatoms on oxygen pressure.

RESULTS

LCMO Film Growth. $La_{5/8}Ca_{3/8}MnO_3$ films of ∼50 unit cells (u.c.) thickness (∼20 nm) were grown by PLD on TiO_2-terminated $SrTiO_3$ (001) (STO) substrates at a temperature of 750 °C as described in the Methods section. We present here results for two background oxygen pressures: 20 mTorr and 50 mTorr. The results for 20 mTorr were reproducible with a lower pressure, 10 mTorr, as well. The growth was monitored *in situ* with use of high-pressure reflection high-energy electron diffraction (RHEED). Immediately after deposition, samples were cooled down to 400 °C at a rate of 150 °C/min in the growth pressure. After that, the deposition chamber was evacuated of oxygen to prevent excessive oxygen adsorption, and samples were quickly transferred *in situ* in UHV into an STM chamber maintained at a pressure $<3 \times 10^{-10}$ Torr for further cooling before imaging. STM imaging was performed at room temperature at an operating pressure $<3 \times 10^{-10}$ Torr in constant current mode. All images presented in the paper were taken with the tip negatively biased in respect to a grounded sample.

Standard *ex situ* X-ray diffraction ω-2θ scans and reciprocal space mapping confirmed epitaxial film growth with pseudocubic (001) film surface and showed that the films are fully strained to the substrate and of a good structural quality. However, the films were not optimized in respect to bulk physical properties. In particular, measurements with a SQUID magnetometer

showed a Curie temperature of about 200 K for films deposited at 50 mTorr of O_2, which is lower than about 260 K in bulk LCMO with the same composition.

The perovskite-like LCMO lattice structure along the pseudocubic [001] direction can be viewed as alternating A-site (La,Ca)O and B-site (MnO_2) layers, and this notation as well as the pseudocubic notation for description of the lattice and surface structures are adapted further in the paper.

The inset in Figure 1 shows an image of a RHEED pattern from the film surface taken in vacuum immediately after film deposition at 50 mTorr. The pattern has strong spots of the zero Laue zone accompanied by weak streaks, which evidence a certain degree of disorder on the film surface. The intensity of the specular spot *versus* time during deposition is shown in the main panel of Figure 1, and exhibits clear oscillations for all 48 layers of the film, characteristic for layer-by-layer growth, with intensity relaxation toward higher values after deposition stop. The RHEED oscillation

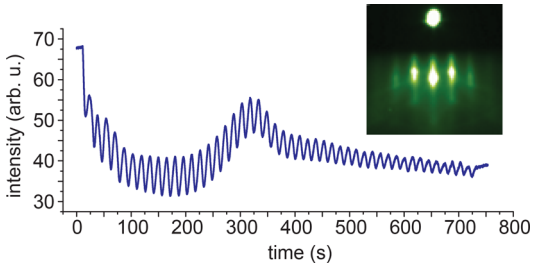

Figure 1. RHEED oscillation of the specular spot for growth at an oxygen background pressure of 50 mTorr. Inset shows a RHEED pattern from the films surface taken shortly after deposition was stopped.

period remains nearly constant during deposition (Figure S1 in Supporting Information) strongly pointing to conservation of substrate termination during film growth.

STM Imaging and Structural Surface Characterization. Figure 2a displays a large-scale STM image of the 50 mTorr film obtained *in situ* at room temperature. In the image, there is a clearly visible vicinal step preserved from the pristine substrate surface. The adjacent terraces are covered by multiple islands as well as holes of similar size corresponding to just started and almost complete layers of the growing film. Figure 2b shows the height distribution in the images of Figure 2a. There are four well-resolved peaks separated by distances close to 200 pm, corresponding to about a half-unit cell. The number of peak pairs indicates the number of full-unit-cell layers simultaneously exposed to the surface, and is equal to three, corresponding to nearly ideal layer-by-layer growth. At the same time, it is apparent that the height distribution indicates a mixed termination of the surface and each peak corresponds to terraces of the same termination, although the terminations take unequal fractions on the surface.

An atomically resolved image of the film surface is shown in Figure 2c. As seen, the surface at the atomic scale consists of two distinctly different structures: one with a disordered appearance in the image and a highly ordered one with a clear $(\sqrt{2} \times \sqrt{2})R45°$ reconstruction. The structures are alternating in average height producing a step-like morphology. The line profile, Figure 2d across the steps along the line in Figure 2c reveals that the average change from one

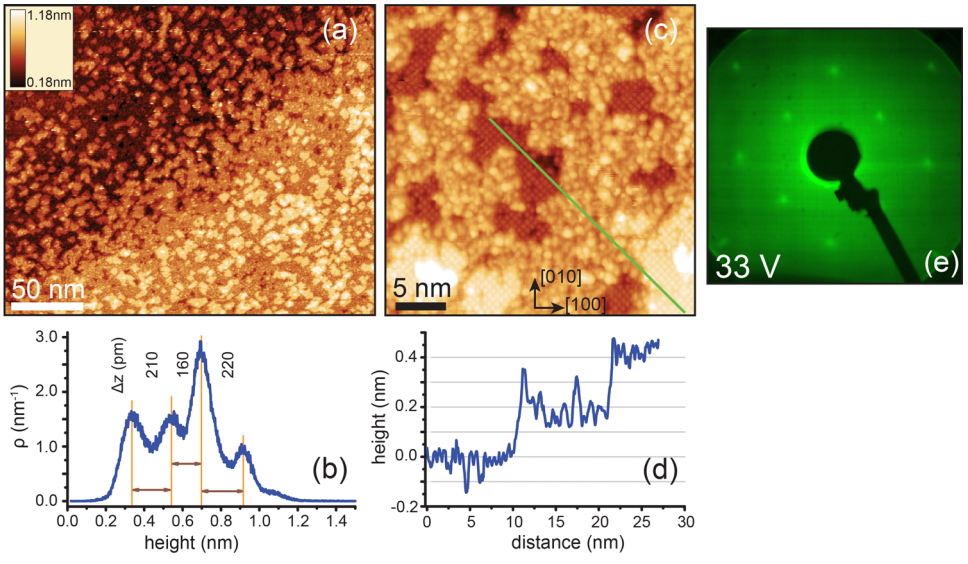

Figure 2. (a) A large-scale STM image of a film surface grown at 50 mTorr oxygen pressure ($V_t = -1.8$ V, $I_t = 55$ pA). (b) A plot of height distribution in the image of panel (a) indicating a mixed termination of the surface. (c) A high-resolution image of the surface in panel (a) revealing a $(\sqrt{2} \times \sqrt{2})R45°$ reconstruction patterns of islands and holes corresponding to one of the terminations and a disordered structure of the other ($V_t = -2$ V, $I_t = 55$ pA). (d) A height profile along the green line in (c) evidencing that the ordered and disordered structures belong to different terminations. (e) A LEED pattern from this sample taken at an acceleration voltage of 33 V; the pattern indicates the $(\sqrt{2} \times \sqrt{2})R45°$ reconstruction.

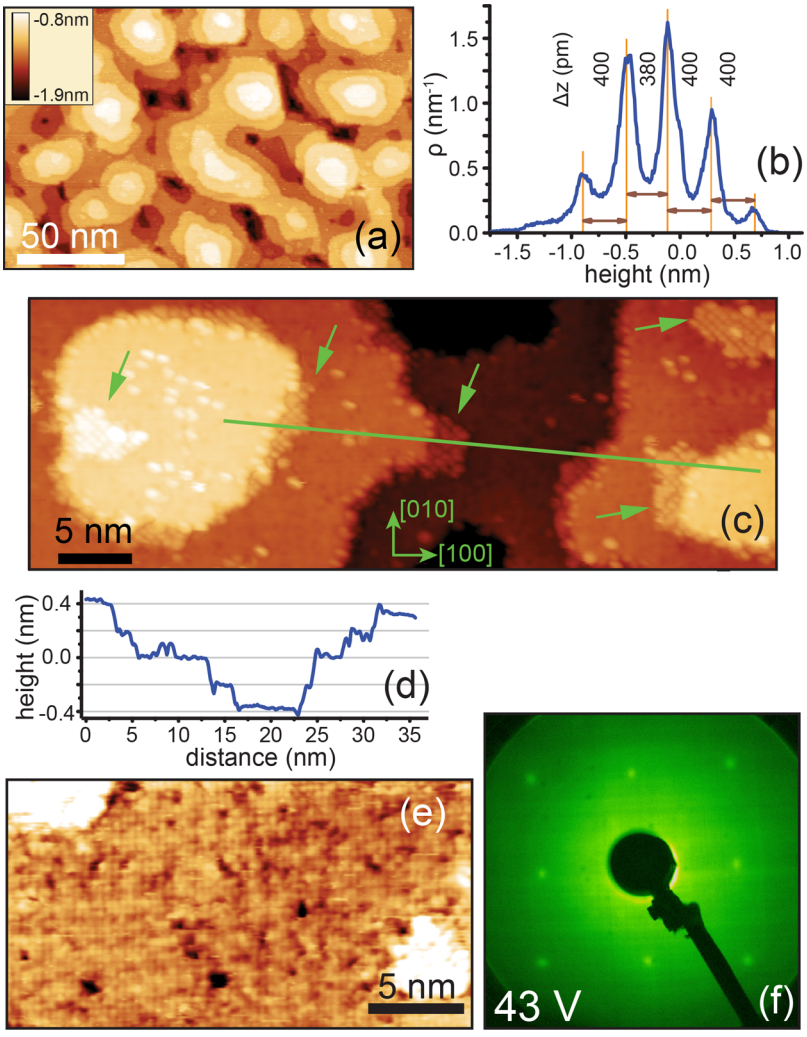

Figure 3. (a) A large-scale STM image of a film surface grown at 20 mTorr oxygen pressure ($V_t = -1.7$ V, $I_t = 48$ pA). (b) A plot of height distribution in the image of panel (a) indicating single termination of the surface. (c) A high-resolution image of the surface in panel (a) revealing ($\sqrt{2} \times \sqrt{2}$)$R45°$ patterns along island edges, which provides evidence for the presence of small areas of the second termination ($V_t = -2$ V, $I_t = 30$ pA). (d) A height profile along the green line in (c). (e) A high-resolution image of a portion of the smooth surface in (c) ($V_t = -0.7$ V, $I_t = 130$ pA). The image clearly shows a (1 × 1) surface. (f) A LEED pattern from this sample taken at an acceleration voltage of 43 V; the pattern indicates an unreconstructed (1 × 1) surface.

structure to the other is close to 200 pm, *i.e.*, one-half unit cell. It can be concluded that the distinctly different surface structures belong to different surface terminations of the perovskite lattice. The termination dominating in the large-scale image (and corresponding to the highest peak in Figure 2b) is disordered in appearance in the high-resolution image. Since the STM is not sensitive to the chemical composition of the surface, the terminations cannot be identified based on STM alone, which would be a key step for understanding the nature of the disorder as well as the reconstruction in the images. To confirm that STM observations are valid for large length scales, we performed a low energy electron diffraction (LEED) characterization of the film surfaces. In agreement with the STM results, LEED showed a sharp ($\sqrt{2} \times \sqrt{2}$)$R45°$ diffraction pattern evidenced by Figure 2e (with the disordered parts of the surface contributing to the diffuse background).

To explore the connection between the observed surface morphology and plume energetics, we have deposited altogether eight films at 50 mTorr of oxygen pressure varying the laser fluence on the target in the range between 0.8 and 2.6 J/cm^2 and, notably, found that, surface morphology seen in Figure 2 is present in the whole range.

As the next step, we performed depositions at a reduced oxygen pressure of $P_{O_2} = 20$ mTorr keeping all other deposition conditions unchanged. Figure 3 displays images obtained from a film deposited at $P_{O_2} =$ 20 mTorr. As seen, the film surface is dramatically different. First, it is covered by terraced mounds of multiple unit cells heights evidencing imperfect layer-by-layer growth (Figure 3a). We note that the RHEED oscillations ceased near the 20th maximum during growth of this film, after which the growth was continued to nominally 50 u.c. thickness based on the time

elapsed from the deposition start and the period of RHEED oscillation at the initial stage of growth. The final RHEED pattern was weak and streaky. The height distribution of the large-scale image in Figure 3b displays only peaks separated by about 400 pm corresponding to terrace steps of one full unit cell height. However, atomically resolved images reveal mixed termination of the surface: there are small portions of a second termination evident from inspection of Figure 3c and d. The minority termination is visible along the island edges in Figure 3c, and again, it shows an ordered $(\sqrt{2} \times \sqrt{2})R45°$ structure similar to the case of the higher deposition pressure. The dominating termination, in contrast, looks smooth and featureless except for a small number of adatoms predominantly grouped at the island edges. It is possible to further resolve the atomic lattice on the majority termination by increasing the tunneling current and moving the tip closer to the surface. As seen in Figure 3e, the surface of the dominant termination is unreconstructed, with a (1×1) structure and a small corrugation <15 pm. LEED showed a clear (1×1) diffraction pattern (Figure 3f); the relative fraction of the $(\sqrt{2} \times \sqrt{2})R45°$ surface was too small to produce a significant spot intensity above background in this case.

An important observation made with STM imaging is that the $(\sqrt{2} \times \sqrt{2})R45°$ surface is common to films deposited at 20 mTorr as well as 50 mTorr. In an earlier work, similar $(\sqrt{2} \times \sqrt{2})R45°$ reconstructed surfaces were observed by Fuchigami *et al.*[38] on the surface of a $La_{5/8}Ca_{3/8}$ MnO_3 film prepared by PLD following a different recipe (with use of ozone during deposition) and were associated with oxygen atoms adsorbed on a B-site (MnO_2) terminated surface. The connection between $(\sqrt{2} \times \sqrt{2})R45°$ structures and adsorbed oxygen was established by Fuchigami *et al.* on the basis of anneals in UHV and in atmosphere of ozone/oxygen mixture, where it was found that the surface structure changes in response to the annealing conditions and sequence. In particular, the $(\sqrt{2} \times \sqrt{2})R45°$ structures could be converted into (1×1) structure by anneals in UHV at 400 °C for 40 min. We conducted similar anneals in UHV with our films, and in contrast to ref 38, the $(\sqrt{2} \times \sqrt{2})R45°$ structures were found to be stable after anneals in UHV up to a temperature of 550 °C for durations up to 90 min. Therefore, we conclude that the $(\sqrt{2} \times \sqrt{2})R45°$ structures on the surface of our films cannot be explained by surface oxygen adsorption.

Before proceeding to the detailed analysis of the surface chemical composition with the goal to identify the film terminations, it should be noted that STM imaging was performed nearly exclusively with a tip negatively biased in respect to a sample, corresponding to an empty-state image. Attempts to perform imaging at positively biased tip were largely unsuccessful. We repeatedly observed that application of a positive bias to the tip during scanning resulted in a transfer of atoms from the sample surface to the tip with loss of imaging stability. Stable imaging could be recovered afterward only by applications of negative-polarity pulses to the tip (up to −4 V amplitude and 30 ms duration). Such pulsing generally resulted in deposition of material on the sample surface. This effect was especially strong while imaging the 50 mTorr films; therefore, its cause should be probably sought in the presence of weakly bound adsorbents, such as oxygen ions and calcium oxide clusters, on the film surface, which can be transferred to the tip by an electric field. However, we repeatedly observed that the $(\sqrt{2} \times \sqrt{2})R45°$ surface is far more accessible for stable imaging both at negative and positive biases without change in overall appearance independently on the bias polarity (Figure S2 in Supporting Information). These suggest that the $(\sqrt{2} \times \sqrt{2})R45°$ surface has significantly less adsorbed species and is more chemically stable.

Angle-Resolved XPS Measurements. In order to clarify the chemical composition of the film surfaces and to identify surface layers exhibiting different structures in the STM images, we employed *in situ* angle-resolved X-ray photoemission spectroscopy (AR-XPS). This surface-sensitive spectroscopic technique was applied in the past with the same purpose to high-temperature superconductors[44] and later to perovskite manganites.[45−47] We collected XPS spectra for a set of different emission angles in respect to the surface normal (polar angles) to probe the film surface composition up to varying depths. Namely, spectra obtained at more gliding angles are more sensitive to the surface composition, and therefore, analysis of spectra as a function of emission angle allows differentiating surface composition from composition of the bulk. For these measurements, samples were rotated along a [100] axis with detection of electrons photoemitted in the (100) plane. The AR-XPS measurements were carried out at room temperature *in situ* soon after completion of the STM work (*i.e.*, within 24−36 h. after sample deposition) following sample transfer in UHV from the STM into an analysis chamber, so that possible surface contamination with carbon and hydrocarbons was minimized. Figure 4 shows the polar angle dependence of the ratios [Mn 2p]/([Ca 2p]+[La 3d]), [O 1s]/([Ca 2p]+[La 3d]), and [Ca 2p]/([Ca 2p]+[La 3d]), where square brackets denote integrated intensities of the corresponding core level peaks normalized as described in the Methods section. The effective attenuation lengths (EAL) for the electron kinetic energies corresponding to these peaks are in the range from about 1.1 to 1.7 nm, which means that the spectra are primarily sensitive to composition within the top 3−4 u. c. of the film for emission along the surface normal, and to somewhat more than 1 u.c. at the polar angle equal to 70 degrees.

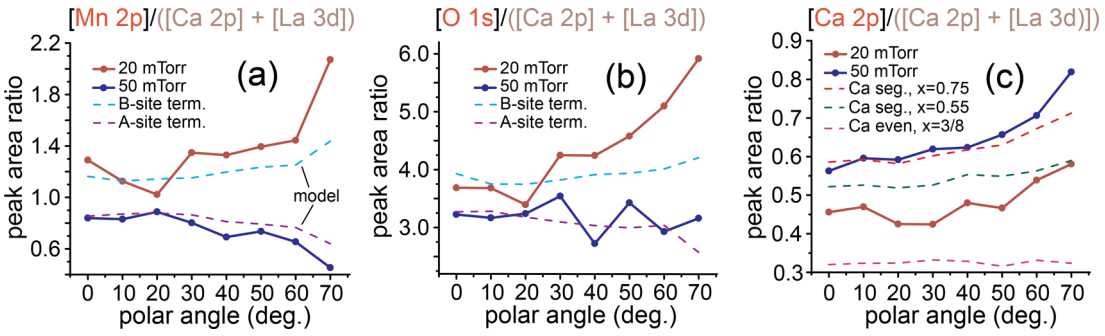

Figure 4. (a) Solid curves are normalized core-level intensity ratios of Mn to (La,Ca), [Mn 2p]/([Ca 2p] + [La 3d]), as functions of the emission polar angle for films deposited at 20 and 50 mTorr of oxygen background pressure. Dashed lines are data obtained with Monte Carlo simulations for the cases of A- and B-site terminations. (b) Same as panel (a) for normalized core-level intensity ratio of O to (La,Ca), [O 1s]/([Ca 2p] + [La 3d]). (c) Solid curves are normalized core-level intensity ratio of Ca to (LaCa), [Ca 2p]/([Ca 2p] + [La 3d]), as functions of the emission polar angle for films deposited at 20 mTorr and 50 mTorr. Dashed lines are data obtained with Monte Carlo simulations for Ca content $x = 0.75$ and $x = 0.55$ in the terminating layer, and for an even distribution of Ca in a film with $x = 3/8$. Square brackets denote normalized intensities of corresponding core-level peaks.

We start the analysis of the AR-XPS data from the angular dependence of the [Mn 2p]/([Ca 2p] + [La 3d]) ratios, because this ratio is most sensitive to the type of the surface termination. Notably, the curves in Figure 4a indicate that the films deposited at 20 mTorr and 50 mTorr exhibit opposite trends for this ratio with increasing polar angle as would be expected from films with different—A- or B-site—terminations.[46,47] Specifically, the ratio [Mn 2p]/([Ca 2p] + [La 3d]) is larger for the film deposited at 20 mTorr and increases at larger polar angles as expected for a predominantly B-site terminated film due to scattering of electrons emitted from Ca and La atoms in the A-site layer under the top B-site layer. In turn, this ratio is smaller in the 50 mTorr film, and it decreases with increasing angle, as would be expected for an A-site terminated film.

Since the oxygen content is different in (La,Ca)O and MnO_2 layers, the ratio [O 1s]/([Ca 2p]+[La 3d]) is also indicative of the surface termination. As seen in Figure 4b, this ratio is increasing with the polar angle in the films deposited at 20 mTorr and smaller with an opposite trend in the 50 mTorr film, the behavior that is expected from B-site and A-site terminated surfaces, respectively.

Angular dependences predicted by the Monte Carlo simulations for fully A-site and B-site terminated films using model structures (described in the Methods section) are also shown in Figure 4a and b. Before discussing the model results in comparison with the experimental data, we should note that the simplified model used does not reproduce all aspects of electron emission in the single-crystalline epitaxial film. In particular, the model takes into account discreteness of the film lattice only along the surface normal, representing atomic layers as amorphous and structureless. Therefore, diffraction effects associated with anisotropic forward scattering as well as atomic-scale details of the surface structure could not be captured in simulations. Diffraction effects,[48] which lead to peak intensity oscillations *vs* emission angle, may contribute up to 30% discrepancy between simulated and experimental intensity ratios at a given emission angle for elements located at unequivalent sites in the crystal lattice. Consequently, the model does not allow distinguishing between *fully* A- or B-site terminated surfaces and *predominantly* A- or B-site terminated surfaces. In the latter case, the XPS will show a weighted average of signals from single-terminated surface areas with statistical weights equal to areal fractions of the terminations.

Bearing this in mind, while simulations correctly reproduce the overall behavior (Figure 4a and b), the simulated data can be used only with this stipulation for estimates and for conclusions based on general trends in the case of [Mn 2p]/([Ca 2p] + [La 3d]) and [O 1s]/([Ca 2p]+[La 3d]) ratios. There is a good agreement between experimental data and calculations for both A- and B-site terminated model structures and both the ratios considered above; the agreement is especially good for the higher-pressure film. Note that the data clearly shows that the films have different terminations, and the higher-pressure film has A-site surface termination. The AR-XPS measurements were performed with several films deposited at 50 mTorr with similar results. However, this is an unexpected result: in all experiments with 50 mTorr depositions, analysis of the RHEED intensity oscillations do not indicate termination conversion during film growth, and consequently, suggest preservation of the substrate B-site termination. This contradiction is further discussed and interpreted in the Discussion section below.

Combining the results of STM and AR-XPS, we unambiguously conclude that the (1 × 1) surface of the 20 mTorr film is MnO_2, and is thus B-site terminated in agreement with the identifications made for STM images of similar LCMO films by Fuchigami *et al.*[38] and Shimizu *et al.*[31] Consequently, the $(\sqrt{2} \times \sqrt{2})R45°$

structure in our films is a signature of an A-site terminated, (La,Ca)O, surface. The nature of the disordered structure in the images of the 50 mTorr films is still to be clarified. On the basis of STM images, the highly ordered $(\sqrt{2} \times \sqrt{2})R45°$ structure is not the dominating termination in the 50 mTorr film, and by exclusion, the disordered structure should be ascribed to B-site termination unless it consists of adsorbed atoms and atomic clusters. Therefore, below we performed further steps in analysis of the AR-XPS data.

We turn to the [Ca 2p]/([Ca 2p]+[La 3d]) ratio, which can be employed to deduce the depth profile of Ca/La ratio in the A-site layers near the surface. (Note that that the measured [Ca 2p]/([Ca 2p]+[La 3d]) ratios are almost insensitive to the surface termination as was verified by Monte Carlo simulations. Also, since La and Ca occupy the same A-type sites in the perovskite lattice, diffraction effects do not affect these ratios.) As seen from the curves in Figure 4c, the [Ca 2p]/([Ca 2p]+[La 3d]) ratios in both films are clearly increasing toward larger polar angles. Since this does not reflect a change in terminations, it evidence instead that Ca is segregated toward the surface in both the cases. Note that the segregation is distinctly stronger in the film deposited at the higher oxygen pressure. Comparison with corresponding curves obtained using the Monte Carlo-simulated spectra allows an estimation of the Ca concentration in the top layer and the degree of segregation. Using the general formula $La_{1-x}Ca_xMnO_3$, we conclude that $x \approx 0.75$ at the surface of the 50 mTorr film. To independently determine the degree of Ca surface segregation, we have also measured splitting of the Mn 3s peak at normal emission for this sample using monochromatic Al K_α X-ray source (Figure S3 in Supporting Information). Splitting of the Mn 3s can be used as an indicator of average Mn valence in Mn compounds.[49] On the basis of the data of ref 50, the measured splitting of $\Delta E_{3s} = 4.8$ eV would correspond to a Mn formal valence of *ca.* 3.6, and assuming oxygen stoichiometry, to Ca content of $x \approx 0.55$. For the used model of Ca concentration profile, this number is close to an average $x \approx 0.52$ in the top three unit cell layers with $x \approx 0.75$ in the terminating unit cell layer. In turn, the estimated surface Ca content in the 20 mTorr film is close to 0.5. These conclusions were verified with use of La 4d core-level peaks with similar results.

To further elucidate the chemical composition of the film surface, we inspected the shapes of individual core level peaks. No differences in peak shapes and positions were found for all peaks regardless of sample and emission angle, with an exception of the O 1s peak. As shown in Figure 5a, the O 1s peaks of the 20 mTorr sample can be deconvoluted in two Gaussian–Lorentzian component peaks independently on the emission angle; addition of a third peak does not improve the fit. However, use of only one peak is

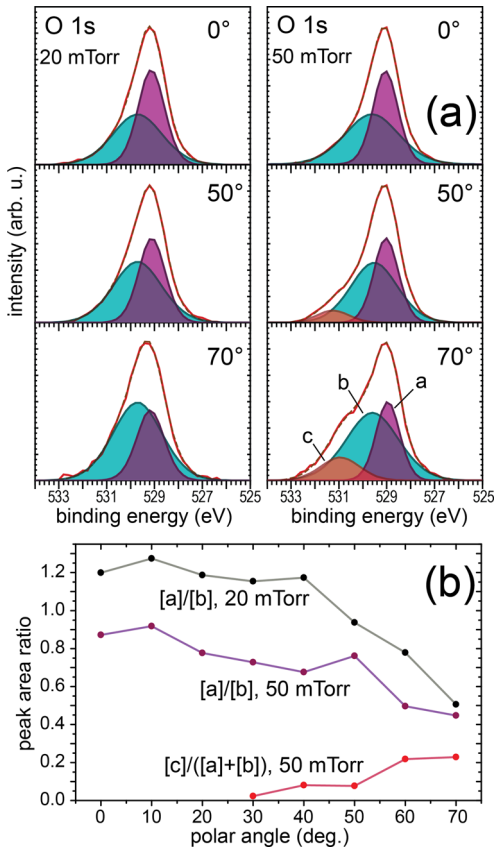

Figure 5. (a) Photoemission spectra of the O 1s state after background correction for films deposited at 20 mTorr (left) and 50 mTorr (right); the spectra were acquired at emission polar angles of 0°, 50°, and 70° (from top to bottom). The peaks were deconvoluted using three Gaussian–Lorentzian components denoted "a", "b", and "c" in the lower right subpanel. (b) O 1s component intensity ratios as functions of emission polar angle. The curve identifications are shown inside the panel. Component lettering is in panel (a).

insufficient to reproduce the peak shape. The two component peaks are a narrower peak at a lower binding energy and a broad peak approximately 0.5 eV higher in binding energy. While the component peak intensity ratio is distinctly dependent on the polar angle as well as the predominant surface termination (Figure 5b), it is apparent that both component peaks should be ascribed to bulk oxygen in the LCMO lattice. On the basis of the larger contribution of the broader peak at greater gliding emission angles, it can be assumed that lattice defect sites contribute to the larger width of higher binding energy component peak as well as inhomogeneities in the Ca distribution along the surface (possibly reflected in the uneven contrast in the image in Figure 3e). The same two component peaks were sufficient to fit the O 1s peaks of the film deposited at 50 mTorr in the spectra obtained at polar angles below 30 degrees. In contrast, at larger angles, a third component peak should be added at a binding energy approximately 1.1 eV higher than the narrow peak for a satisfactory fit. The presence of the third component is especially clear from the high

binding energy shoulder of the O 1s peak at 70 degrees. The spectral weight of the third component greatly increases with increasing emission angle, from <10% at angles below 50° to about 20% at 70°, indicating that this component peak originates from some form of surface oxygen, similarly to the conclusion made for a close XPS peak structure in a work with fractured single crystals of LSMO by Mannella *et al.*[51]

Taking into account the larger Ca segregation revealed by AR-XPS in this sample, oxygen can be bound with Ca in loose CaO clusters on the surface. Such clusters may be of extrinsic origin, forming in the laser plasma plume at the larger background oxygen pressure, which seems to be suggested by the STM images of the 20 mTorr and 50 mTorr films. Hence, we have additionally inspected the corresponding Ca 2p peaks to examine this possibility. In the literature,[52,53] higher binding energy satellite shoulders were observed at the Ca 2p core-level peak in samples with a large density of defects and with a strong Ca segregation on the surface. In particular, Choi *et al.*[53] observed Ca 2p peaks with higher-binding energy satellites in $La_{0.9}Ca_{0.1}MnO_3$ films, which were attributed to surface Ca segregation and associated defects. No such higher-binding-energy satellites were found at the Ca 2p peaks of all our measured samples, independent of the sample and emission angle (see Figure S4 in Supporting Information). The lack of such peaks strongly points to absence of any significant amount CaO clusters on films surfaces, and therefore, we conclude that amount of Ca not incorporated in the lattice is negligible in our films. In addition, the analysis above indicates that the amount of adsorbed atomic oxygen on the (1 × 1) surface (of the 20 mTorr film) is also negligible, correlating well with results of high-resolution STM imaging by Fuchigami *et al.*[38]

DISCUSSION

We turn here to possible interpretations of the combined RHEED, STM and AR-XPS results. It can be concluded that that the disordered areas seen in the STM image of the 50 mTorr film largely consist of small—few unit cells in lateral dimensions—islands of incomplete MnO_2 layer. The layer can viewed as having multiple cation and/or anion vacancies and, therefore, a significant degree of structural and electronic disorder, details of which are difficult to resolve in STM (this is more evident from rare filled state images such as in Figure S2b in Supporting Information). On the basis of the analysis of the corrugation height over the disordered termination in a large number of STM images, we exclude a scenario, when the atoms of the top B-site termination tend to "pile" into three-dimensional island after the deposition stops. Apparently, the structural imperfection of the top B-site layers does not prevent the lateral growth of (La,Ca)O islands on top so that the growth occurs in the effectively layer-by-layer mode. It can be assumed that the MnO_2 layer structure develops to a nearly perfect one as it becomes buried in the course of the further growth. (However, the defects may become incorporated in the bulk of the films during growth as well.) This agrees both with RHEED behavior and with the AR-XPS results. Indeed, the small two-dimensional islands on top attenuate the flux of electrons photoemitted by the underlying A-site layer less as compared to a continuous layer. Additionally, STM images show that the fraction of the large-area exposed A-site termination is much larger than that for the film deposited at a lower pressure. Overall, this leads a predominantly A-site surface termination seen in the AR-XPS measurements of the 50 mTorr films. The defect-rich MnO_2 surface may readily adsorb oxygen after deposition stop, which is in part responsible for the disordered appearance of the B-site termination in the STM images and the instability of the STM imaging at positive tip biases mentioned above.

On the basis of these conclusions, we speculate that the film growth process can be described as formation of continuous A-site islands on top of a B-site layer due to a higher mobility of Ca and La on the B-site terminated surface. MnO_2 islands nucleate on top of (La,Ca)O islands; however, the number and size of B-site islands depend on the mobility of Mn adatoms, which is a strong function of oxygen pressure, with higher mobility at a lower pressure. The layer-by-layer growth occurs in a way that it is "led" by (La,Ca)O half unit-cell planes with B-site (MnO_2) half unit-cell islands being formed on top. Generally, this growth mode should result in mixed termination of the films. At a higher pressure, lower mobility of Mn adatoms causes a relatively higher degree of atomic scale disorder in MnO_2 planes, even though the growth proceeds in a nearly ideal layer-by-layer fashion. Giving a higher mobility of Mn adatoms, a lower oxygen pressure leads to a significantly smoother film surface at the atomic scale. The finding of the varying degree of a mixed termination may also explain contradictory conclusions about the type of the termination in similar LSMO films in literature.[41,48,54,55] We note here that our analysis reveals that care must be taken in ascribing terminations based on RHEED data alone; the fact of a B-site terminated substrate and the appearance of a layer-by-layer growth cannot be taken as indicative of a B-site terminated film. Further, though well-known in theoretical works on RHEED,[56] the oscillation maxima themselves do not correspond to complete layer growth, and the possibility of mixed terminations exists, even when the film deposition is stopped at the RHEED intensity maximum.

The exact coupling mechanism between Mn adatom mobility and oxygen pressure cannot be resolved based on the results reported here and requires further work.

The higher mobility can be a consequence of a higher average kinetic energy of the species in the plasma plume at a lower background pressure. A sharp transition in the growth mode and film surface morphology over background oxygen pressure was previously reported for PLD of related complex oxides, *e.g.*, $SrRuO_3$ in ref 57 and $La_{0.7}Sr_{0.3}MnO_3$ in ref 58. In the latter case, the transition was attributed to pressure dependence of the so-called "plume range" (*i.e.*, the distance from the target, at which species in the laser plume start to be thermalized due to interaction with a background gas[59,60]) and interpreted in the framework of the structure-zone model of Thornton,[61] which provides a simple phenomenological link between film morphology and energy of incoming particles. However, our results, especially independence of the surface structure at P_{O_2} = 50 mTorr on the laser fluence in a broad range from 0.8 to 2.6 J/cm^2, suggest that the picture is more complicated, and other effects not captured by this interpretation should be considered. In particular, an additional possibility is that a lower oxygen content of the A-site layer at a lower background pressure, modifies the surface lattice constant and, consequently, modifies the energy barriers for adatom motion on the surface.

At this point, the question about the nature of the $(\sqrt{2} \times \sqrt{2})R45°$ reconstruction on the A-site-terminated surface remains open and requires a further work as well to be clarified. The reconstruction can be driven by the electrostatic energy associated with the (partially) polar LCMO (001) surface. We note also that the A-site planes have a rock salt structure, which should be under a large, 8−10%, tensile strain in respect to the bulk three-dimensional rock salt lattice. The observed reconstruction can be a pathway to accommodate this strain. Further, we cannot rule out the possibility that the observed reconstruction can be associated with the regular pattern of Jahn−Teller distortions, similar to the pattern produced by the charge-ordered state as observed by STM on the surface of a $Bi_{1-x}Ca_xMnO_3$ single crystal.[32]

One more important fact revealed by our AR-XPS measurements is a smaller degree of surface Ca segregation at the reduced oxygen pressure during deposition. This result indicates a trend which is opposite to that found for Sr surface segregation in $La_{0.7}Sr_{0.3}MnO_3$ in response to changes in oxygen pressure during anneals.[62] Cation segregation at the surface is common in perovskite oxides, and in particular in $LaA'MnO_3$ (A′ = Ca, Sr, Ba) thin films.[37,45,63,64] The exact nature of the segregation is currently under debate; however, multiple driving forces can be of a different degree of importance depending on concrete internal and external factors. They may include reduction of surface energy due to reconfiguration of chemical bonds, reduction of lattice strain caused by cation size difference, as well as electrostatic interactions between charged cations, vacancies, and the space charge near polar surfaces or interfaces of polar perovskite oxides. Reduction of lattice elastic energy by redistribution of cations with different ionic radii across the film thickness is most frequently invoked as a driving mechanism of the segregation in thin films. In the case of LCMO films on STO, the tensile epitaxial strain drives large La^{3+} ions toward the film/substrate interface, facilitating segregation of smaller Ca^{2+} at the film surface. The oxygen deficiency results in increase of the film lattice constant, which also provides a driving force for Ca segregation at the film surface. Experimentally, Ca segregation was reported on surfaces of LCMO films deposited by PLD as well as by magnetron sputtering.[45,65] Taking into account a short time of film exposure to high temperatures after deposition stop, Ca segregation found in our films should be viewed as a highly dynamic process occurring during films growth. Among the factors mentioned above, we consider dynamic reduction of the electrostatic component of the surface energy as the most probable reason for Ca segregation in our films. Transport of Ca^{2+} ions toward surface can evolve trough reshuffling with atoms of the layer on top, similar to the processes uncovered by Lee *et al.*[66] in growth of layered oxide films. This may explain the discrepancy in the trend of dopant segregation *vs* oxygen pressure as compared to the annealed films, mentioned earlier in this paragraph.

CONCLUSION

To summarize, we have implemented *in situ* atomically resolved STM imaging in combination with *in situ* angle-resolved XPS measurement to get access to atomic structure and chemical composition of $La_{5/8}Ca_{3/8}MnO_3$ films grown by PLD. On the basis of our results, we conclude that the growth process proceeds through formation of islands of A-site termination with subsequent nucleation and growth of B-site termination layer on top. This growth mode generally leads to double-termination of the film surface, with B-site termination being predominant with a varying fraction, even when growth is formally close to the ideal layer-by-layer. The results reveal a strong effect of the background oxygen pressure during deposition on the features of the film surface and chemical composition. The reduction of the oxygen pressure from 50 to 20 mTorr results in a transition of the surface structure from disordered with a relatively large fraction of A-site termination to nearly perfectly ordered at the atomic scale with only a small fraction of A-site termination. This reveals the oxygen pressure is an important factor for an accurate control of the surface termination. We speculate that the observations can be explained by influence of the oxygen background on mobility of Mn adatoms. AR-XPS measurements showed as well that Ca surface segregation is decreased with reduction of

oxygen pressure. Additionally, our analysis reveals that the fact of a B-site terminated substrate and the appearance of a layer-by-layer growth in the RHEED cannot be taken *per se* as indicative of a B-site terminated film. Further work is needed to clarify the mechanisms underlying the observed effects.

METHODS

Film Growth. LCMO films of 50 u.c. (~20 nm) thickness were grown by PLD on TiO_2-terminated $SrTiO_3$ (001) substrates using a commercial stoichiometric $La_{5/8}Ca_{3/8}MnO_3$ ceramic target. To obtain single termination, STO substrates were etched in buffered oxide etch solution (pH = 4.5) for 30 s and annealed in air for 4 h at 900 °C. Prior to film deposition, each substrate was inspected with AFM in tapping mode using the AFM tip oscillation phase signal for detection of second (SrO) termination on the substrate surface. Only substrates with a low surface roughness and a negligible fraction of the minor—SrO—termination were selected for film depositions with following STM experiments. Terrace width on the substrates was in the range from about 200 to 400 nm. Substrate temperature during deposition was kept at 750 °C. Background oxygen pressures used were 10, 20, and 50 mTorr. Laser fluence (KrF laser, $\lambda = 248$ nm) was kept at about 1 J/cm^2 at pressures 10 and 20 mTorr, and was varied between 0.8 and 2.6 J/cm^2 at an oxygen pressure of 50 mTorr. Pulsed repetition frequencies were of 5 or 10 Hz (without noticeable difference in results). The target-substrate distance was 70 mm. The growth was monitored *in situ* with use of high-pressure reflection high-energy electron diffraction (RHEED) with the incident beam along the [100] azimuth of the substrate. The substrates were attached to stainless steel plates with a very small amount of silver paint and were heated during deposition by an infrared laser from the plate side. The amount of the silver paint was sufficiently small to avoid contamination of the film surface with silver.[67] Immediately after deposition, samples were cooled down without changing oxygen pressure at a rate of 150 °C/min down to a temperature of 400 °C. After that, the deposition chamber was evacuated of oxygen to prevent excessive surface oxygen adsorption, and samples were quickly transferred *in situ* in UHV into an STM chamber maintained at a pressure $<3 \times 10^{-10}$ Torr for further cooling to room temperature before imaging. In order to verify the bulk composition of the films, we deposited 100 nm thick films on STO substrates and used energy dispersive X-ray spectroscopy (EDX) to determine the film bulk composition. The EDX showed that cation composition in the films matches that of the target within the uncertainty of the measurements of about ±5 at. %.

STM Imaging. STM imaging was performed *in situ* at room temperature with an Omicron VT system at an operating pressure $<3 \times 10^{-10}$ Torr using mechanically cut Pt/Ir tips in constant current mode. All images presented in the paper were taken with the tip negatively biased in respect to a grounded sample. Imaging with negative bias with this setup probes the empty electronic states. We have STM-imaged altogether more than 20 films with highly reproducible results.

XPS Measurements. The angular resolved XPS measurements were carried out at room temperature *in situ* right after completion of the STM work (*i.e.*, within 24−36 h. after sample deposition) following sample transfer in UHV into an analysis chamber, so that possible surface contamination with carbon and hydrocarbons was minimized. The measurements were performed with the nonmonochromatic Al Kα radiation ($h\nu$ = 1486.6 eV) from a SPECS XR50 Mg/Al double-anode X-ray source operated at 280 W using a SPECS PHOIBOS 150 hemispherical electron energy analyzer at room temperature in UHV at a base pressure $<8 \times 10^{-11}$ Torr. To take the spectra, samples were rotated along a [100] axis to vary the emission polar angle (the angle in respect to the surface normal) along the [010] azimuth. The spot size of the natural X-ray source in our XPS system is some 3 mm in diameter, while the sample width is 5 mm. This combination may result in a significant flux of electrons emitted from the sample holder and substrate sides, with a larger relative contribution at larger polar angles. To avoid this parasitic effect, the analyzer lens was set to medium magnification mode with an appropriately chosen entrance slit (0.5 mm × 20 mm), so that the sample view size projected on the analyzer aperture (and visible to the detector) was restricted to about 0.1 mm in the direction normal to the sample rotation axis. The analyzer entrance diaphragm was set to limit the collection angle to ±2° (as follows from analyzer specifications provided by the manufacturer). Under these settings, spurious signals were minimized to a negligibly low level, as was verified with a control sample made of a sputter-cleaned Cu foil cut in the shape of a substrate and fixed on an identical sample holder. In the control experiments, an edge of the Cu foil was moved across the view field of the spectrometer at different polar angles, and a Cu emission peak was recorded. The analyzer work function was calibrated using a sputter-cleaned polycrystalline silver foil. For high-resolution scans over selected peaks, the pass energy was set to 60 eV.

XPS Data Processing. AR-XPS data were processed using CasaXPS v.2.3.16 software. Peak intensities were determined as areas under the peaks after subtraction of the Shirley background and normalization to respective core level photoionization cross sections (relative sensitivity factors) and analyzer transmission factors. We used the analyzer transmission function provided by the analyzer manufacturer in the analysis of the spectra. The parameter "MFP Exponent" in CasaXPS (taking into account the energy dependence of the electron mean free path) was set to zero for calculations of the peak intensity ratios, so that the values were uncorrected for the electron mean free path for proper comparison with the numerically simulated data. The model spectra in Figure 4 were calculated using a NIST Standard Reference Database 100 (SESSA),[68] which contains a Monte Carlo simulation module along with a computer expert system for quantitative interpretations of XPS spectra. The simulated spectra were processed in CasaXPS in the same way as experimental ones. The films were modeled as stacks of alternating 193 pm-thick layers with chemical compositions and densities corresponding to (La,Ca)O and MnO_2 planes of the LCMO structure, as shown by an example model in Figure S5 in Supporting Information. This model mimics the analytical model used in ref 45 with exponential decay of the Ca concentration x from surface to the bulk value. Primary to the Monte Carlo simulations, we used the analytical model for estimations of Ca surface concentration and of concentration decay length to approximate the experimental data. The Monte Carlo-simulated curves shown in Figure 4 were obtained with a Ca content $x = 3/8$ in the A-site layers located more than 3 u.c. away from the surface. To calculate concentrations in the top second and third A-site layers of the Monte Carlo model, the decay lengths in the analytical model were set to 0.5 u.c. and 0.15 u.c. for $x = 3/4$ and $x = 0.55$ at the surface, respectively. The effective attenuations lengths (EAL) for the electron kinetic energies corresponding to analyzed peaks were determined from the NIST Standard Reference Database 82.[69]

Conflict of Interest: The authors declare no competing financial interest.

Acknowledgment. This research was sponsored by the U.S. Department of Energy, Office of Science, Basic Energy Sciences, Materials Sciences and Engineering Division (A.T., R.K.V., A.G.G., T.L.M., H.N.L., S.V.K.). Research was conducted at CNMS, which also provided support (A.P.B., M.D.B., L.Q., P.G.) and which is sponsored at Oak Ridge National Laboratory by the U.S. Department of Energy, Office of Basic Energy Sciences, Scientific User Facilities Division.

Supporting Information Available: Additional figures showing RHEED oscillation period *vs* deposition time, a filled-state STM image, XPS Mn 3s and Ca 2p core level peaks, and an

example of SESSA model layout. This material is available free of charge *via* the Internet at http://pubs.acs.org.

REFERENCES AND NOTES

1. Tokura, Y. Critical Features of Colossal Magnetoresistive Manganites. *Rep. Prog. Phys.* **2006**, *69*, 797.
2. Coey, J. M. D.; Viret, M.; von Molnár, S. Mixed-Valence Manganites. *Adv. Phys.* **2009**, *58*, 571–697.
3. Dagotto, E.; Hotta, T.; Moreo, A. Colossal Magnetoresistant Materials: The Key Role of Phase Separation. *Phys. Rep.* **2001**, *344*, 1–153.
4. Ahn, C. H.; Triscone, J. M.; Mannhart, J. Electric Field Effect in Correlated Oxide Systems. *Nature* **2003**, *424*, 1015–1018.
5. Ahn, K. H.; Lookman, T.; Bishop, A. R. Strain-Induced Metal-Insulator Phase Coexistence in Perovskite Manganites. *Nature* **2004**, *428*, 401–404.
6. Ichikawa, H.; Nozawa, S.; Sato, T.; Tomita, A.; Ichiyanagi, K.; Chollet, M.; Guerin, L.; Dean, N.; Cavalleri, A.; Adachi, S.; *et al.* Transient Photoinduced 'Hidden' Phase in a Manganite. *Nat. Mater.* **2011**, *10*, 101–105.
7. Xiong, Z. H.; Wu, D.; Vardeny, Z. V.; Shi, J. Giant Magnetoresistance in Organic Spin-Valves. *Nature* **2004**, *427*, 821–824.
8. Yamada, H.; Ogawa, Y.; Ishii, Y.; Sato, H.; Kawasaki, M.; Akoh, H.; Tokura, Y. Engineered Interface of Magnetic Oxides. *Science* **2004**, *305*, 646–648.
9. Dörr, K. Ferromagnetic Manganites: Spin-Polarized Conduction *Versus* Competing Interactions. *J. Phys. D: Appl. Phys.* **2006**, *39*, R125.
10. Barraud, C.; Seneor, P.; Mattana, R.; Fusil, S.; Bouzehouane, K.; Deranlot, C.; Graziosi, P.; Hueso, L.; Bergenti, I.; Dediu, V.; *et al.* Unravelling the Role of the Interface for Spin Injection into Organic Semiconductors. *Nat. Phys.* **2010**, *6*, 615–620.
11. Garcia, V.; Bibes, M.; Bocher, L.; Valencia, S.; Kronast, F.; Crassous, A.; Moya, X.; Enouz-Vedrenne, S.; Gloter, A.; Imhoff, D.; *et al.* Ferroelectric Control of Spin Polarization. *Science* **2010**, *327*, 1106–1110.
12. Harada, T.; Ohkubo, I.; Lippmaa, M.; Sakurai, Y.; Matsumoto, Y.; Muto, S.; Koinuma, H.; Oshima, M. Spin-Filter Tunnel Junction with Matched Fermi Surfaces. *Phys. Rev. Lett.* **2012**, *109*, 076602.
13. Yi, D.; Liu, J.; Okamoto, S.; Jagannatha, S.; Chen, Y. C.; Yu, P.; Chu, Y. H.; Arenholz, E.; Ramesh, R. Tuning the Competition between Ferromagnetism and Antiferromagnetism in a Half-Doped Manganite through Magnetoelectric Coupling. *Phys. Rev. Lett.* **2013**, *111*, 127601.
14. Yu, X. Z.; Tokunaga, Y.; Kaneko, Y.; Zhang, W. Z.; Kimoto, K.; Matsui, Y.; Taguchi, Y.; Tokura, Y. Biskyrmion States and Their Current-Driven Motion in a Layered Manganite. *Nat. Commun.* **2014**, *5*, 3198.
15. Moreno, C.; Munuera, C.; Valencia, S.; Kronast, F.; Obradors, X.; Ocal, C. Reversible Resistive Switching and Multilevel Recording in $La_{0.7}Sr_{0.3}MnO_3$ Thin Films for Low Cost Nonvolatile Memories. *Nano Lett.* **2010**, *10*, 3828–3835.
16. Sun, C.; Hui, R.; Roller, J. Cathode Materials for Solid Oxide Fuel Cells: A Review. *J. Solid State Electrochem.* **2010**, *14*, 1125–1144.
17. Kourkoutis, L. F.; Song, J. H.; Hwang, H. Y.; Muller, D. A. Microscopic Origins for Stabilizing Room-Temperature Ferromagnetism in Ultrathin Manganite Layers. *Proc. Natl. Acad. Sci. U. S. A.* **2010**, *107*, 11682–11685.
18. Sun, J. Z.; Abraham, D. W.; Rao, R. A.; Eom, C. B. Thickness-Dependent Magnetotransport in Ultrathin Manganite Films. *Appl. Phys. Lett.* **1999**, *74*, 3017–3019.
19. Calderón, M. J.; Brey, L.; Guinea, F. Surface Electronic Structure and Magnetic Properties of Doped Manganites. *Phys. Rev. B: Condens. Matter Mater. Phys.* **1999**, *60*, 6698–6704.
20. Freeland, J. W.; Gray, K. E.; Ozyuzer, L.; Berghuis, P.; Badica, E.; Kavich, J.; Zheng, H.; Mitchell, J. F. Full Bulk Spin Polarization and Intrinsic Tunnel Barriers at the Surface of Layered Manganites. *Nat. Mater.* **2005**, *4*, 62–67.
21. Nourafkan, R.; Capone, M.; Nafari, N. Surface Polaron Formation in the Holstein Model. *Phys. Rev. B: Condens. Matter Mater. Phys.* **2009**, *80*, 155130.
22. Nourafkan, R.; Marsiglio, F. Competition between Reduced Delocalization and Charge Transfer Effects for a Two-Band Hubbard Model. *Phys. Rev. B: Condens. Matter Mater. Phys.* **2011**, *84*, 075133.
23. Lepetit, M.-B.; Mercey, B.; Simon, C. Interface Effects in Perovskite Thin Films. *Phys. Rev. Lett.* **2012**, *108*, 087202.
24. Bibes, M.; Balcells, L.; Valencia, S.; Fontcuberta, J.; Wojcik, M.; Jedryka, E.; Nadolski, S. Nanoscale Multiphase Separation at $La_{2/3}Ca_{1/3}MnO_3/SrTiO_3$ Interfaces. *Phys. Rev. Lett.* **2001**, *87*, 067210.
25. Pilania, G.; Gao, P.-X.; Ramprasad, R. Establishing the $LaMnO_3$ Surface Phase Diagram in an Oxygen Environment: An *Ab Initio* Kinetic Monte Carlo Simulation Study. *J. Phys. Chem. C* **2012**, *116*, 26349–26357.
26. Katsuya, I.; Takeo, O.; Ryota, S.; Tomihiro, H.; Taro, H. Atomically Resolved Surface Structure of $SrTiO_3$ (001) Thin Films Grown in Step-Flow Mode by Pulsed Laser Deposition. *Appl. Phys. Express* **2010**, *3*, 075701.
27. Ohsawa, T.; Iwaya, K.; Shimizu, R.; Hashizume, T.; Hitosugi, T. Thickness-Dependent Local Surface Electronic Structures of Homoepitaxial $SrTiO_3$ Thin Films. *J. Appl. Phys.* **2010**, *108*, 073710.
28. Shin, J.; Borisevich, A. Y.; Meunier, V.; Zhou, J.; Plummer, E. W.; Kalinin, S. V.; Baddorf, A. P. Oxygen-Induced Surface Reconstruction of $SrRuO_3$ and Its Effect on the $BaTiO_3$ Interface. *ACS Nano* **2010**, *4*, 4190–4196.
29. Tselev, A.; Ganesh, P.; Qiao, L.; Siemons, W.; Gai, Z.; Biegalski, M. D.; Baddorf, A. P.; Kalinin, S. V. Oxygen Control of Atomic Structure and Physical Properties of $SrRuO_3$ Surfaces. *ACS Nano* **2013**, *7*, 4403–4413.
30. Ohsawa, T.; Shimizu, R.; Iwaya, K.; Hitosugi, T. Visualizing Atomistic Formation Process of SrO_x Thin Films on $SrTiO_3$. *ACS Nano* **2014**, *8*, 2223–2229.
31. Shimizu, R.; Ohsawa, T.; Iwaya, K.; Shiraki, S.; Hitosugi, T. Epitaxial Growth Process of $La_{0.7}Ca_{0.3}MnO_3$ Thin Films on $SrTiO_3$(001): Thickness-Dependent Inhomogeneity Caused by Excess Ti Atoms. *Cryst. Growth Des.* **2014**, *14*, 1555–1560.
32. Renner, C.; Aeppli, G.; Kim, B. G.; Soh, Y.-A.; Cheong, S. W. Atomic-Scale Images of Charge Ordering in a Mixed-Valence Manganite. *Nature* **2002**, *416*, 518–521.
33. Rößler, S.; Padmanabhan, B.; Elizabeth, S.; Bhat, H. L.; Steglich, F.; Wirth, S. Atomically Resolved Scanning Tunneling Microscopy on Perovskite Manganite Single Crystals. *Appl. Phys. Lett.* **2010**, *96*, 202512.
34. Rønnow, H. M.; Renner, C.; Aeppli, G.; Kimura, T.; Tokura, Y. Polarons and Confinement of Electronic Motion to Two Dimensions in a Layered Manganite. *Nature* **2006**, *440*, 1025–1028.
35. Bryant, B.; Renner, C.; Tokunaga, Y.; Tokura, Y.; Aeppli, G. Imaging Oxygen Defects and Their Motion at a Manganite Surface. *Nat. Commun.* **2011**, *2*, 212.
36. Mathur, N.; Littlewood, P. Mesoscopic Texture in Manganites. *Phys. Today* **2003**, *56*, 25–30.
37. Lee, W.; Han, J. W.; Chen, Y.; Cai, Z.; Yildiz, B. Cation Size Mismatch and Charge Interactions Drive Dopant Segregation at the Surfaces of Manganite Perovskites. *J. Am. Chem. Soc.* **2013**, *135*, 7909–7925.
38. Fuchigami, K.; Gai, Z.; Ward, T. Z.; Yin, L. F.; Snijders, P. C.; Plummer, E. W.; Shen, J. Tunable Metallicity of the $La_{5/8}Ca_{3/8}MnO_3$(001) Surface by an Oxygen Overlayer. *Phys. Rev. Lett.* **2009**, *102*, 066104.
39. Song, J. H.; Susaki, T.; Hwang, H. Y. Enhanced Thermodynamic Stability of Epitaxial Oxide Thin Films. *Adv. Mater.* **2008**, *20*, 2528–2532.
40. Huijben, M.; Martin, L. W.; Chu, Y. H.; Holcomb, M. B.; Yu, P.; Rijnders, G.; Blank, D. H. A.; Ramesh, R. Critical Thickness and Orbital Ordering in Ultrathin $La_{0.7}Sr_{0.3}MnO_3$ Films. *Phys. Rev. B: Condens. Matter Mater. Phys.* **2008**, *78*, 94413.
41. Li, Z.; Bosman, M.; Yang, Z.; Ren, P.; Wang, L.; Cao, L.; Yu, X.; Ke, C.; Breese, M. B. H.; Rusydi, A.; *et al.* Interface and Surface Cation Stoichiometry Modified by Oxygen Vacancies in Epitaxial Manganite Films. *Adv. Funct. Mater.* **2012**, *22*, 4312–4321.
42. Boschker, J. E.; Folven, E.; Monsen, Å. F.; Wahlström, E.; Grepstad, J. K.; Tybell, T. Consequences of High Adatom

Energy During Pulsed Laser Deposition of $La_{0.7}Sr_{0.3}MnO_3$. *Cryst. Growth Des.* **2012**, *12*, 562566.
43. Choi, W. S.; Rouleau, C. M.; Seo, S. S. A.; Luo, Z.; Zhou, H.; Fister, T. T.; Eastman, J. A.; Fuoss, P. H.; Fong, D. D.; Tischler, J. Z.; *et al.* Atomic Layer Engineering of Perovskite Oxides for Chemically Sharp Heterointerfaces. *Adv. Mater.* **2012**, *24*, 6423–6428.
44. Frank, G.; Ch, Z.; Göpel, W. Surface Composition of Clean, Epitaxial Thin Films of $YBa_2Cu_3O_{7-x}$ from Quantitative X-Ray Photoemission Spectroscopy Analysis. *Phys. Rev. B: Condens. Matter Mater. Phys.* **1991**, *43*, 2828–2834.
45. Choi, J.; Zhang, J.; Liou, S. H.; Dowben, P. A.; Plummer, E. W. Surfaces of the Perovskite Manganites $La_{1-x}Ca_xMnO_3$. *Phys. Rev. B: Condens. Matter Mater. Phys.* **1999**, *59*, 13453–13459.
46. Kumigashira, H.; Horiba, K.; Ohguchi, H.; Ono, K.; Oshima, M.; Nakagawa, N.; Lippmaa, M.; Kawasaki, M.; Koinuma, H. *In Situ* Photoemission Characterization of Terminating-Layer-Controlled $La_{0.6}Sr_{0.4}MnO_3$ Thin Films. *Appl. Phys. Lett.* **2003**, *82*, 3430–3432.
47. Loviat, F.; Rønnow, H. M.; Renner, C.; Aeppli, G.; Kimura, T.; Tokura, Y. The Surface Layer of Cleaved Bilayer Manganites. *Nanotechnology* **2007**, *18*, 044020.
48. Raisch, C.; Langheinrich, C.; Werner, R.; Kleiner, R.; Koelle, D.; Glaser, M.; Chassé, T.; Chassé, A. X-Ray Photoelectron Diffraction Study of Dopant Effects in $La_{0.7}X_{0.3}MnO_3$ (X = La, Sr, Ca, Ce) Thin Films. *J. Appl. Phys.* **2013**, *113*, 063511.
49. Galakhov, V.; Demeter, M.; Bartkowski, S.; Neumann, M.; Ovechkina, N.; Kurmaev, E.; Lobachevskaya, N.; Ya, M.; Mitchell, J.; Ederer, D. Mn 3s Exchange Splitting in Mixed-Valence Manganites. *Phys. Rev. B: Condens. Matter Mater. Phys.* **2002**, *65*, 113102.
50. Beyreuther, E.; Grafström, S.; Eng, L.; Thiele, C.; Dörr, K. XPS Investigation of Mn Valence in Lanthanum Manganite Thin Films under Variation of Oxygen Content. *Phys. Rev. B: Condens. Matter Mater. Phys.* **2006**, *73*, 155425.
51. Mannella, N.; Rosenhahn, A.; Nambu, A.; Sell, B. C.; Mun, B. S.; Yang, S. H.; Marchesini, S.; Watanabe, M.; Ibrahim, K.; Ritchey, S. B.; *et al.* Surface Characterization of Colossal Magnetoresistive Manganites $La_{1-x}Sr_xMnO_3$ Using Photoelectron Spectroscopy. *J. Electron Spectrosc. Relat. Phenom.* **2006**, *153*, 37–57.
52. Taguchi, H.; Shimada, M. X-Ray Photoelectron Spectroscopy Study of $(Ca_{1-x}La_x)MnO_{2.97}$ ($0.1 \leq X \leq 0.4$). *J. Solid State Chem.* **1987**, *67*, 37–41.
53. Choi, J.; Dulli, H.; Liou, S. H.; Dowben, P. A.; Langell, M. A. The Influence of Surface Terminal Layer and Surface Defects on the Electronic Structure of CMR Perovskites: $La_{0.65}A_{0.35}MnO_3$ (A = Ca, Sr, Ba). *Phys. Status Solidi B* **1999**, *214*, 45–57.
54. Bertacco, R.; Contour, J. P.; Barthélemy, A.; Olivier, J. Evidence for Strontium Segregation in $La_{0.7}Sr_{0.3}MnO_3$ Thin Films Grown by Pulsed Laser Deposition: Consequences for Tunnelling Junctions. *Surf. Sci.* **2002**, *511*, 366–372.
55. Poggini, L.; Ninova, S.; Graziosi, P.; Mannini, M.; Lanzilotto, V.; Cortigiani, B.; Malavolti, L.; Borgatti, F.; Bardi, U.; Totti, F.; *et al.* A Combined Ion Scattering, Photoemission, and DFT Investigation on the Termination Layer of a $La_{0.7}Sr_{0.3}MnO_3$ Spin Injecting Electrode. *J. Phys. Chem. C* **2014**, *118*, 13631–13637.
56. Shin, B.; Aziz, M. J. Modeling RHEED Intensity Oscillations in Multilayer Epitaxy: Determination of the Ehrlich-Schwoebel Barrier in Ge(001) Homoepitaxy. *Phys. Rev. B: Condens. Matter Mater. Phys.* **2007**, *76*, 165408.
57. Yoo, Y. Z.; Chmaissem, O.; Kolesnik, S.; Dabrowski, B.; Maxwell, M.; Kimball, C. W.; McAnelly, L.; Haji-Sheikh, M.; Genis, A. P. Contribution of Oxygen Partial Pressures Investigated over a Wide Range to $SrRuO_3$ Thin-Film Properties in Laser Deposition Processing. *J. Appl. Phys.* **2005**, *97*, 103525.
58. Koubaa, M.; Haghiri-Gosnet, A. M.; Desfeux, R.; Lecoeur, P.; Prellier, W.; Mercey, B. Crystallinity, Surface Morphology, and Magnetic Properties of $La_{0.7}Sr_{0.3}MnO_3$ Thin Films: An Approach Based on the Laser Ablation Plume Range Models. *J. Appl. Phys.* **2003**, *93*, 5227–5235.
59. Geohegan, D. B. Physics and Diagnostics of Laser Ablation Plume Propagation for High-T_c Superconductor Film Growth. *Thin Solid Films* **1992**, *220*, 138–145.
60. Strikovski, M.; Miller, J. H. Pulsed Laser Deposition of Oxides: Why the Optimum Rate Is About 1 Å Per Pulse. *Appl. Phys. Lett.* **1998**, *73*, 1733–1735.
61. Thornton, J. A. The Microstructure of Sputter-Deposited Coatings. *J. Vac. Sci. Technol., A* **1986**, *4*, 3059–3065.
62. Fister, T. T.; Fong, D. D.; Eastman, J. A.; Baldo, P. M.; Highland, M. J.; Fuoss, P. H.; Balasubramaniam, K. R.; Meador, J. C.; Salvador, P. A. *In Situ* Characterization of Strontium Surface Segregation in Epitaxial $La_{0.7}Sr_{0.3}MnO_3$ Thin Films as a Function of Oxygen Partial Pressure. *Appl. Phys. Lett.* **2008**, *93*, 151904.
63. Bowen, M.; Bibes, M.; Barthélémy, A.; Contour, J.-P.; Anane, A.; Lemaître, Y.; Fert, A. Nearly Total Spin Polarization in $La_{2/3}Sr_{1/3}MnO_3$ from Tunneling Experiments. *Appl. Phys. Lett.* **2003**, *82*, 233–235.
64. Infante, I. C.; Sánchez, F.; Fontcuberta, J.; Wojcik, M.; Jedryka, E.; Estradé, S.; Peiró, F.; Arbiol, J.; Laukhin, V.; Espinós, J. P. Elastic and Orbital Effects on Thickness-Dependent Properties of Manganite Thin Films. *Phys. Rev. B: Condens. Matter Mater. Phys.* **2007**, *76*, 224415.
65. Simon, J.; Walther, T.; Mader, W.; Klein, J.; Reisinger, D.; Alff, L.; Gross, R. Diffusion and Segregation Effects in Doped Manganite/Titanate Heterostructures. *Appl. Phys. Lett.* **2004**, *84*, 3882–3884.
66. Lee, J. H.; Luo, G.; Tung, I. C.; Chang, S. H.; Luo, Z.; Malshe, M.; Gadre, M.; Bhattacharya, A.; Nakhmanson, S. M.; Eastman, J. A.; *et al.* Dynamic Layer Rearrangement During Growth of Layered Oxide Films by Molecular Beam Epitaxy. *Nat. Mater.* **2014**, *13*, 879–883.
67. Tselev, A.; Vasudevan, R. K.; Kalinin, S. V.; Baddorf, A. P. Effect of Silver Doping on the Surface of $La_{5/8}Ca_{3/8}MnO_3$ Epitaxial Films. *Appl. Phys. Lett.* **2014**, *105*, 101602.
68. National Institute of Standards and Technology Standard Reference Database 100: NIST Database for the Simulation of Electron Spectra for Surface Analysis (SESSA): Version 1.3, Gaithersburg, Maryland, USA. http://www.nist.gov/srd/nist100.cfm.
69. National Institute of Standards and Technology Standard Reference Database 82, Verstion 1.3, Gaithersburg, Maryland, USA. http://www.nist.gov/srd/nist82.cfm.